remote sensing

MDPI

Article

Automatic Delineation of Water Bodies in SAR Images with a Novel Stochastic Distance Approach

Andrea Rey [1,*], Natalia Revollo Sarmiento [2], Alejandro César Frery [3] and Claudio Delrieux [2]

[1] Department of Mathematics and Signal and Image Processing Center, Facultad Regional Buenos Aires, Universidad Tecnológica Nacional, Medrano 951, Ciudad Autónoma de Buenos Aires C1179, Argentina
[2] Electric and Computer Engineering Department, Universidad Nacional del Sur, and National Scientific and Technical Research Council (CONICET), Bahía Blanca B8000, Argentina
[3] School of Mathematics and Statistics, Victoria University of Wellington, Wellington 6140, New Zealand
* Correspondence: arey@frba.utn.edu.ar

Abstract: Coastal regions and surface waters are among the fundamental biological and social development resources worldwide. For this reason, it is essential to thoroughly monitor these regions to determine and characterize their geographical features and environmental health. These geographical regions, however, present several monitoring challenges when using remotely sensed imagery. Small water bodies tend to be surrounded by swamps, marshes, or vegetation, making accurate border detection difficult. Coastal waters, in turn, experience several phenomena due to winds, undercurrents, and waves, which also hamper the detection of environmental hazards like oil spills. In this work, we propose an automated segmentation algorithm that can be applied to these targets in airborne and spaceborne SAR images. The method is based on pointwise detection in fuzzy borders using a parameter estimation of the $\mathcal{G}^0$ distribution, which has been successfully used in similar contexts. The underlying assumption is that the sought-for border separates regions with different textures, each having different distribution parameters. Then, stochastic distances can identify the most likely point where this parameter change occurs. A curve interpolation algorithm then estimates the actual contour of the body given the detected points. We assess the adequacy of eight stochastic distances that are mostly applied in the literature. We evaluate the performance of our method in terms of similarity between true and detected boundaries on simulated and actual SAR images, achieving promising results. The performance of our proposal is assessed by Hausdorff distance and Intersection over Union. In the case of synthetic data, the selection of the best stochastic distance depends on the parameters of the $\mathcal{G}_I^0$ distribution. In contrast, the harmonic-mean and triangular distances produced the best results in detecting borders in three actual SAR images of lagoons. Finally, we present the results of our proposal applied to an image with oil spills using Bhattacharyya, Hellinger, and Jensen–Shannon distances.

Keywords: Border detection; segmentation; water bodies; SAR images; stochastic distances

check for updates

Citation: Rey, A.; Revollo Sarmiento, N.; Frery, A.C.; Delrieux, C. Automatic Delineation of Water Bodies in SAR Images with a Novel Stochastic Distance Approach. *Remote Sens.* **2022**, *14*, 5716. https://doi.org/10.3390/rs14225716

Academic Editors: Luis Gómez Déniz, María Elena Buemi and Nelson Monzón López

Received: 9 October 2022
Accepted: 10 November 2022
Published: 12 November 2022

1. Introduction

Coastal and surface waters are vital environmental resources in ecological systems and for human activities such as agriculture, industrial production, public health and safety, tourism, and human life settlement. Although there is no strict definition to the concept of a small water body, it has been used in the literature to consider small lakes, ponds, low-order streams, ditches, and springs [1]. Small water bodies play a fundamental role in providing habitats for animals and plants, and their environmental interaction generates beneficial weather conditions. Understanding surface water bodies' behavior is crucial in water resources assessment, weather conditions modeling, crop improvement, flood mitigation, aquifer monitoring, wetland recording, and ecosystems studies, among many others. Coastal waters, in turn, are the interface between complex

geographic and geomorphologic environments, giving rise to unique ecological systems. A large proportion of human settlements and activities are very close to coastal regions, exerting potentially or actually negative anthropic effects. Thus, adequate monitoring of these regions is essential to understand and mitigate these adverse effects.

Traditional monitoring and surveying techniques to acquire relevant information are known to be costly and cumbersome, and for this reason remote sensing has emerged as a feasible option since it produces adequate spatial and temporal information about the Earth's surface. Optical satellite imagery provides satisfactory spectral information, which facilitates land cover determination, among other purposes. However, freely available satellite imagery usually lacks fine enough spatial and temporal resolution for small water body monitoring, or for the determination of small targets, e.g., oil spills, and also strongly depends on adequate daylight and weather conditions during acquisition. Synthetic Aperture Radar (SAR) sensors, in turn, emit active microwave pulses and then sense the energy that bounces back, with which it is possible to obtain backscatter information of the surface, regardless of daylight or weather conditions, and with arbitrary spatial resolution. SAR sensors can also "see" through canopy and vegetation layers, which is also necessary during an accurate detection of the actual surface of shallow water bodies (fresh or coastal), whose surface may be obscured by vegetation, either natural (mangroves, swamps, marshes, to name a few) or in waterlogged fields (rice crops, sugar cane, willows, and birches).

Water is characterized by a high dielectric constant that affects the backscatter intensity. Since SAR sensors can detect differences in geometric and dielectric properties, this technology appears adequate for studying surface water bodies, which can be distinguished in SAR images as dark regions. Data provided by SAR sensors have been widely used in recent years to detect and extract water patterns and to quantify their changes [2–10].

Another vital area of research concerns the detection of oil spills in water. According to the European Space Agency (ESA), the coastal environment is being damaged because of tanker accidents and illegal ship discharges that spill large amounts of oil into the sea. One of the major problems is the difficulty in identifying the whole affected area, the degree of smoothness, and the direction of its movement. Oil spills are a threat to naval activity, human beings, and animal life, and they are of interest in public, political, and scientific fields. Since the speed of oil slicks ranges from 0.4 cm^{-1} to 0.75 cm^{-1} [11], a timely detection methodology is crucial to prevent pollution and preserve natural resources.

SAR sensors also have the advantage of producing images of difficult to access zones, being a tool widely used in oil spill detection [12]. However, this kind of image shows patches such as eddies, upwelling, internal waves, rain cells, and wind shadows, which are oil lookalikes but not actual oil features [13]. Both phenomena appear as black spots in SAR images. Moreover, supervised algorithms face the problem of the scarcity of training samples [14]. One of the most popular and simple techniques used in this task is visual inspection and manual delineation [15], whose reliability strongly depends on the expertise and experience of personnel trained in photointerpretation. So far, the lack of robust identification techniques still raises the requirement of professionally trained supervision [16]. In this sense, semi-automatic methods can be a good complement, alleviating the burden of humanly supervised tasks.

Unsupervised processing is advantageous over human-assisted processing, being less expensive and less affected by the typical human inaccuracies that arise due to fatigue, distractions, and other factors [17,18]. A notable disadvantage of human-assisted detection in this application domain is the difficulties and intra- and intersubject variance of the human vision in distinguishing fuzzy boundaries. These issues increase the execution costs and times, and demand more than one operator to achieve trustworthy results [19]. In this context, edges play a fundamental role in image processing and computer vision. Although usually understood as *"changes in intensity or color along a border"*, the notion of an edge can be more general. Edges are important because they can be used as simple descriptors of complex objects. Blake and Isard [20] discussed

their importance in applications that range from robotics to computer-based animation. In particular, in remote sensing applications, edge detection allows for fast delineation of features of interest as, for instance, shores. Detected edges can be later refined and used as feature descriptors in high-level interpretation procedures. Even though edges behave locally as lines, in some cases, there are only transition zones (fuzzy edges), which are relevant in the cases considered in this work. Most edge detection techniques employ local operators, i.e., operations that enclose a small region around each image position. In other words, the evidence of edge occurrence is assessed on a spatially limited region around each point. Remarkable examples of this approach are the Laplacian, Marr–Hildreth, and Canny operators, which find features as approximations of the unobserved continuous image gradient [21].

Gambini et al. [22] proposed a novel approach, (here termed "Gambini Algorithm" or GA). They analyzed a thin strip of pixels, finding evidence of a change of textural properties along the strip in an iterative fashion. If the strip crosses an edge between regions with different characteristics, the border is where such differences are maximal. The original proposal used the likelihood of univariate amplitude SAR data under the $\mathcal{G}^0$ model and obtained excellent results even in the presence of strong noise levels [23]. This statistical line-search approach was then extended to fully polarimetric SAR data [24]. Although very successful in some cases, in this approach, the border detection depends on computing a likelihood function several times, thus imposing a heavy computational burden. Nascimento et al. [25] used stochastic distances between PolSAR samples in the GA approach, obtaining excellent results while reducing the computational cost. Naranjo-Torres et al. [26] used a different class of distances, namely geodesic measures, on intensity data. This was the first attempt to use distances between intensity samples in the GA. It was computationally affordable and successful for SAR images with one or two looks (very noisy images).

Figure 1 shows a chronological overview of the use of the three main components that characterize an edge detection approach using GA, namely: (i) the model (the $\mathcal{G}^0$ model, its Harmonic $\mathcal{G}^0_{\mathrm{H}}$ version, the Wishart distribution $\mathcal{W}$, or distribution-free as in Ref. [27]); (ii) the type of data (Amplitude, Intensity, Polarimetric); and (iii) the function to maximize (likelihood, non-parametric tests S_{NP}, geodesic distances d_{G}, or features derived from H-ϕ divergences d^H_ϕ). This figure also shows this paper's contribution, namely the use of intensity data under the $\mathcal{G}^0$ model and a statistical test based on d^H_ϕ divergences.

Nascimento et al. [28] used stochastic distances between intensity samples. Stochastic distances were not used in the GA until Revollo et al. [29] proposed a technique to detect oil spills based on change detection over data strips. The expressions in [28] are more general than the geodesic distance and produce a wealth of distances that can be turned into statistical tests. In some cases, they rely on numerical integration.

The novelty of our approach is to combine the GA with a hypothesis test whose statistic is defined, for intensity data, in terms of stochastic distances derived from the d^H_ϕ-family of divergences. Gambini et al. [22] used probabilities to detect edges at distances no larger than k pixels from the correct position. This quantitative measure is present in all subsequent studies. Instead, we propose a different quality assessment evaluating two measures, the Hausdorff distance between the estimated and actual edges and the Intersection over Union (IoU) of the corresponding areas. These measures are more relevant to the problem we are dealing with. Moreover, we also analyze the impact of the number of strips on the results, and propose a technique which adapts this parameter. Finally, we use eight stochastic distances and evaluate their performance with simulated and actual imagery. We tackle two problems, namely the recognition of oil spills and of water bodies boundaries with a unified approach. Both aim at delineating boundaries between targets with disparate (often unseen) properties, and suffer from different sources of confusion. The former, by waves and low wind; the latter, by shadows. Our solution relies on statistical features that are little disturbed by these issues.

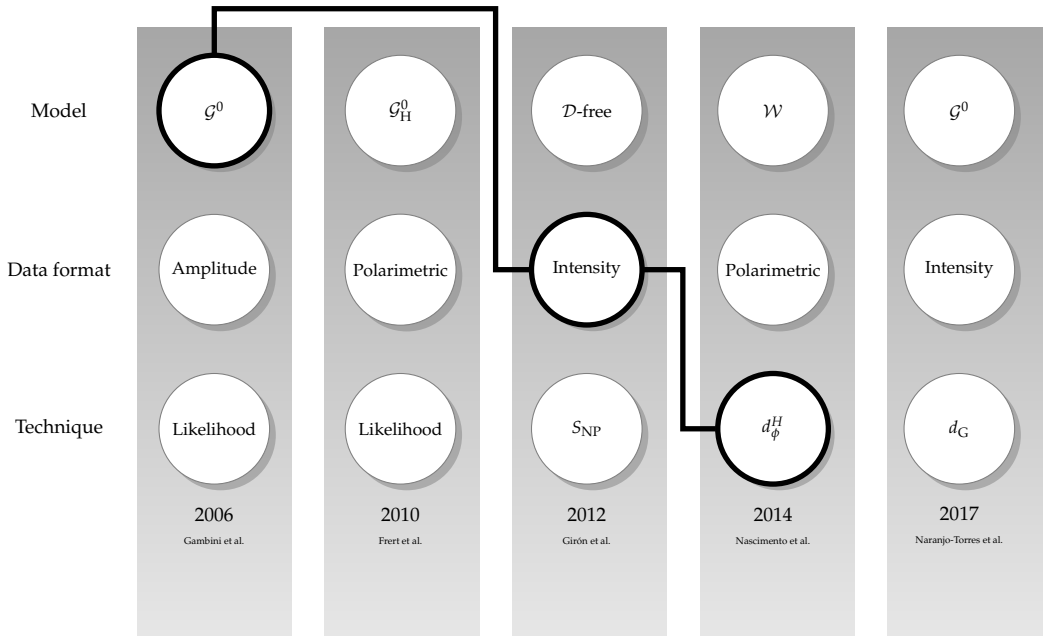

Figure 1. Chronological overview of the main edge detection approaches in SAR imagery using the Gambini Algorithm [22,24–27]. The contribution of this work is shown in bold lines.

This manuscript unfolds as follows. Section 2 describes the required theory, including the multiplicative model (Section 2.1) and hypothesis tests based on stochastic divergences (Sections 2.2 and 2.3). Section 3 is devoted to the methodology; the proposed algorithm is presented in Section 3.1, and the test cases are described in Section 3.2. In Section 4 we present results obtained with simulated data and images from an operational sensor. Section 5 concludes the article with an analysis of the results.

2. Theoretical Framework

2.1. Multiplicative Model

The analysis of SAR images is challenging due to the presence of *speckle*, a non-additive, non-Gaussian interference process that arises during the image formation. The multiplicative model is one of the most successful statistical descriptions of this data. The intensity of the SAR data is a random variable Z, called *return*. Under the multiplicative model, it is the product of two independent random variables: X, the actual *backscatter* and Y, the speckle. See further details in Ref. [30]. The family of $\mathcal{G}^0_I$ distributions was introduced in Ref. [31] as a model devised to understand and quantify the statistical parameters of local regions in SAR images. This distribution arises assuming that X can be modeled by an Inverse Gamma distribution, $X \sim \Gamma^{-1}(\alpha, \gamma)$, with texture parameter $\alpha < 0$ and scale parameter $\gamma > 0$. Multilook speckle can always be described as a Gamma distribution with shape parameter $L \geq 1$ (the number of looks) and unitary mean, denoted $Y \sim \Gamma(L, L)$. Then, the distribution of Z is characterized by the probability density function

$$f_Z(z; \alpha, \gamma, L) = \frac{L^L \Gamma(L - \alpha)}{\gamma^\alpha \Gamma(-\alpha)\Gamma(L)} z^{L-1} (\gamma + Lz)^{\alpha - L} \mathbb{1}_{\mathbb{R}_+}(z), \tag{1}$$

in which $-\alpha, \gamma > 0$ and $L \geq 1$. This situation is denoted as $Z \sim \mathcal{G}^0_I(\alpha, \gamma, L)$.

Given the random sample $\mathbf{Z} = (Z_1, Z_2, \ldots, Z_n)$, and assuming that L is known, the likelihood function for (α, γ) is

$$\mathcal{L}(\alpha, \gamma; \mathbf{Z}) = \left[\frac{L^L \Gamma(L - \alpha)}{\gamma^\alpha \Gamma(-\alpha)\Gamma(L)} \right]^n \prod_{i=1}^n Z_i^{L-1} (\gamma + LZ_i)^{\alpha - L}. \tag{2}$$

The maximum likelihood estimator (MLE) is commonly employed to estimate α, γ due to its optimal asymptotic properties [32]. Moreover, the number of looks can be estimated as the reciprocal square of the coefficient of variation on data with fully developed speckle, as in Ref. [33]:

$$\widehat{L} = \left[\frac{\overline{\boldsymbol{Z}'}}{sd(\boldsymbol{Z}')} \right]^2, \tag{3}$$

using $\boldsymbol{Z}'$, samples from textureless areas where $\alpha \to -\infty$, e.g., pastures and bare soil, and it can be assumed fixed for the whole image, and denoting its sample mean and sample standard deviation as $\overline{\boldsymbol{Z}'}$ and $sd(\boldsymbol{Z}')$, respectively. Alternatively, the user may use the nominal number of looks (which we do not recommend, as it is usually an optimistic measure of quality), or a regression model to estimate L.

2.2. Stochastic Divergences and Distances

We recall here the main stochastic divergences which form the statistical tests for the hypothesis of changes in properties. Without loss of generality, let U and V be two continuous random variables defined over the same probability space with the same support $\mathcal{R} \subseteq \mathbb{R}$, and with densities $f_U(u;\theta_U)$ and $f_V(v;\theta_V)$ where θ_U and θ_V are the parameter vectors. Consider the functions $\phi, H\colon \mathbb{R}_{>0} \to \mathbb{R}_{\geq 0}$ satisfying that ϕ is convex and H is strictly increasing with $H(0) = 0$. The (H,ϕ)-divergence [34] between f_U and f_V is

$$D_\phi^H(U,V) = H\left(\int_{\mathcal{R}} \phi\left(\frac{f_U(x;\theta_U)}{f_V(x;\theta_V)} \right) f_V(x;\theta_V) dx \right). \tag{4}$$

Since the triangular inequality does not necessarily hold [35], this measure is not a metric in the strict sense. Even though some of them are not even symmetric, a possible solution is to consider the distances

$$d_\phi^H(U,V) = \frac{D_\phi^H(U,V) + D_\phi^H(V,U)}{2}. \tag{5}$$

Table 1 shows some H and ϕ functions that give rise to well-know divergences. The last column is the constant $\tau = (H'(0)\phi''(1))^{-1}$, which will be used later.

Table 1. Stochastic divergences and their H-ϕ functions.

Name	H	ϕ	τ
Arithmetic-geometric	x	$[(x+1)/2]\log[(x+1)/(2x)]$	4
Bhattacharyya	$-\log(1-x)$	$(x+1)/2 - \sqrt{x}$	4
Hellinger	$x/2$	$(\sqrt{x}-1)^2$	4
Harmonic-mean	$-\log(1-x/2)$	$(x-1)^2/(x+1)$	2
Jensen–Shannon	x	$x\log[2x/(x+1)]$	4
Kullback–Leibler	x	$x\log x$	1
Rényi	$\log[(\beta-1)x+2]/(\beta-1)$	$[x^\beta - \beta(x-1) - 2]/(\beta-1)$, $0<\beta<1$	β^{-1}
Triangular	x	$(x-1)^2/(x+1)$	1

Some well-known measures arise with the following selection of H and ϕ in the previous symmetrized versions:

Arithmetic-geometric (AG) [36]

$$d_{\mathrm{AG}}(U,V) = \frac{1}{2} \int (f_U + f_V) \log \frac{f_U + f_V}{2\sqrt{f_U f_V}}. \tag{6}$$

Bhattacharyya (B) [37]

$$d_{\mathrm{B}}(U,V) = -\log \sqrt{f_U f_V}. \tag{7}$$

Hellinger (H) [38]

$$d_{\mathrm{H}}(U,V) = 1 - \int \sqrt{f_U f_V}. \tag{8}$$

Harmonic mean (HM) [39]

$$d_{\mathrm{HM}}(U,V) = -\log \int \frac{2 f_U f_V}{f_U + f_V}. \tag{9}$$

Jensen–Shannon (JS) [40]

$$d_{\mathrm{JS}}(U,V) = \frac{1}{2}\left[\int f_U \log \frac{2 f_U}{f_U + f_V} + \int f_V \log \frac{2 f_V}{f_U + f_V}\right]. \tag{10}$$

Kullback–Leibler (KL) [41]

$$d_{\mathrm{KL}}(U,V) = \frac{1}{2}\int (f_U - f_V) \log \frac{f_U}{f_V}. \tag{11}$$

Rényi (R) [42] of order $0 < \beta < 1$

$$d_{\mathrm{R}}^{\beta}(U,V) = \frac{1}{\beta - 1} \log\left[\frac{1}{2}\left(\int f_U^{\beta} f_V^{1-\beta} + \int f_U^{1-\beta} f_V^{\beta}\right)\right]. \tag{12}$$

Triangular (T) [39]

$$d_{\mathrm{T}}(U,V) = \int \frac{(f_U - f_V)^2}{f_U + f_V}. \tag{13}$$

Although interesting and widely used in the literature, these distances do not have intrinsic interpretability and are not comparable. The work by Salicrú et al. [34] solves both issues by turning them into test statistics with the same asymptotic distribution.

2.3. Hypothesis Test

The most frequent comparison is between samples with the same distribution, possibly indexed by different parameters. Let U and V be such random variables, whose distributions are characterized by the densities $f(u;\theta_U)$ and $f(v;\theta_V)$ with parameter vectors in $\Theta \subset \mathbb{R}^M$. In this case, the distance between them can be indicated by $d_{\phi}^{h}(\theta_U, \theta_V)$. We are interested in testing the null hypothesis $H_0 : \theta_U = \theta_V$ using the samples $\boldsymbol{U} = (U_1, U_2, \ldots, U_m)$ from U and $\boldsymbol{V} = (V_1, V_2, \ldots, V_n)$ from V. Salicrú et al. [34] proved that, under H_0,

$$S_{\phi}^{H}(\widehat{\theta}_U, \widehat{\theta}_V) = \frac{2mn\tau}{m+n} d_{\phi}^{H}(\widehat{\theta}_U, \widehat{\theta}_V) \tag{14}$$

converges to a χ^2_M-distributed random variable, where $\widehat{\theta}_U$ and $\widehat{\theta}_V$ are the maximum likelihood estimators based on $\boldsymbol{U}$ and $\boldsymbol{V}$, respectively, provided $m, n \to \infty$ at the same rate. Table 1 provides the values of τ for each case. This result holds for a large class of H-ϕ functions, particularly for all the ones defined in Section 2.2.

The null hypothesis is, thus, rejected with significance level η, if

$$\Pr\left(\chi^2_M \geq S_{\phi}^{H}(\widehat{\theta}_U, \widehat{\theta}_V)\right) \leq \eta.$$

Such a rejection, or the p-value associated to the samples, is our indicator of a change of properties: our estimator of the edge location.

When this test is applied to an image, it provides a statistical tool to refute the claim that the same distribution can model two samples obtained from different regions.

3. Methodology

3.1. Algorithm to Detect Boundary Pixels

We consider a specific region of interest (ROI) within the image, which is selected by the user and which should include a small water body such as a lake, seawater, or similar. This target should be approximately centered on the RoI. In order to apply the proposed algorithm, a pixel $c = (x_c, y_c)$ is fixed as a rotation center and a number of rays or strips n_r is set. Since n_r also sets the number of detected points in the border, the selection of an adequate value for this parameter should be based on a balance between a significant number of points to find the border's approximating curve and the required computational cost. First, a segment of pixels $\bar{s}$ is built using Bresenham's algorithm [43] from the initial point c to the final point $(w, 1)$ (above right corner), where w and h indicate respectively the width and height of the ROI. Let $dx = (w - x_c)$ and $dy = (h - y_c)$. For simplicity, it is assumed that $w > h$, meaning a slope $dy/dx < 1$. If $(x, y) \in \bar{s}$, the next pixel $\mathrm{px}_{\mathrm{next}}$ in the segment is chosen from the decision parameter $\Delta = 2dy - dx$ as follows:

$$\mathrm{px}_{\mathrm{next}} = \begin{cases} (x+1, y) & \text{if } \Delta \leq 0 \text{ (below the true line)}, \\ (x+1, y+1) & \text{if } \Delta > 0 \text{ (above the true line)}, \end{cases} \tag{15}$$

and the decision parameter is updated as:

$$\Delta_{\mathrm{updated}} = \begin{cases} \Delta + 2dy & \text{if } \Delta \leq 0, \\ \Delta + 2(dy - dx) & \text{if } \Delta > 0. \end{cases} \tag{16}$$

This process is replicated for $x = x_c, \ldots, w$. In case the slope is greater than 1, the methodology is analogous but the sampling is made using the coordinate y.

From the segment $\bar{s} = \{(x_i, y_i)\}$, it is considered that the ray strip $\bar{S} \in \mathbb{Z}^{\#\bar{s} \times 6}$ such that the ith row of $\bar{S}$ is of the form $(\mathrm{px}_{i,-1}, \mathrm{px}_{i,0}, \mathrm{px}_{i,1})$ where $\mathrm{px}_{i,j} = (x_i, y_i + j)$ and $\#\bar{s}$ denote the number of pixels in the segment. Then, the ray strip is rotated with center c and angle $\theta_k = 2\pi k/n_r$, for $k = 1, 2, \ldots, n_r$, producing a set of ray strips formed by elements $\bar{S}_k \in \mathbb{Z}^{\ell_k \times 6}$ whose ith row is of the form $(\mathrm{px}'_{i,-1}, \mathrm{px}'_{i,0}, \mathrm{px}'_{i,1})$ where $\mathrm{px}'_{i,j}$ is the rotation of $\mathrm{px}_{i,j}$. The number of rows ℓ_k is determined by the fact that $\bar{S}_k$ must lie in the image. The number of looks is estimated using (3), and one of the stochastic distances from (6)–(13) is selected and indicated by d in what follows.

For every rotated ray strip $\bar{S}_k$, let $z_{i,j}$ be the intensity value of the pixel $\mathrm{px}'_{i,j}$. Thus, $z_{i,j}$ is the ith row of the array of intensity values $\mathbf{z} \in \mathbb{R}^{\ell_k \times 3}$. For each $p = 10, \ldots, \ell_k - 10$, the set of intensity values is divided into two samples: $s_1 = \{z_{i,j} : i = 1, \ldots, p \wedge j = 1, 2, 3\}$ and $s_2 = \{z_{i,j} : i = p+1, \ldots, \ell_k \wedge j = 1, 2, 3\}$. The MLE $\widehat{\theta}^a = (\widehat{\alpha}_a, \widehat{\gamma}_a)$ is computed using the sample s_a for $a = 1, 2$. The selected stochastic distance $d(\widehat{\theta}^1, \widehat{\theta}^2)$ is allocated in a vector of distances. Then, suppose $p_{\max}$ is the value of p that maximizes these distances. In this case, we split the ray strip about this point, and consider the two sample sets at each side of the strip, for which the statistic test (14) is computed to apply the hypothesis test introduced in Section 2.3. Then, if the null hypothesis is rejected, the pixel $(x_{p_{\max}}, y_{p_{\max}})$ is considered a part of an edge. This approach is summarized in Algorithm 1.

Algorithm 1: Algorithm for estimating the edge points.

Input:
- d a stochastic distance `// from (6)-(13)`
- n_r number of rays
- $c = (x_c, y_c)$ centre of rotation

Output: Set of detected points
Data: ROI of a SAR image

```
L ← estimated number of looks // using (3)
w ← ROI width
h ← ROI height
if h > w then
    ROI ← transpose of ROI
    w ← ROI width
    h ← ROI height
s̄ ← {(x_i, y_i)} points in the segment from c to (w, h) // using Bresenham's algorithm
S̄ ← array of size #s̄ × 6 // #s̄ number of pixels in s̄
S̄[i,] ← (x_i   y_i − 1   x_i   y_i   x_i   y_i + 1)
for k = 1, 2, ..., n_r do
    S̄_k ← rotation of S̄ with center c and angle 2πk/n_r
for each S̄_k do
    ℓ_k ← number of rows of S̄_k
    z ← {z_{i,j} : i = 1, ..., ℓ_k ∧ j = 1, 2, 3} intensity values of the pixels in S_k
    for each p ∈ 10 : ℓ_k − 10 do
        s_1 ← {z_{i,j} : i = 1, ..., p ∧ j = 1, 2, 3} first sample
        s_2 ← {z_{i,j} : i = p + 1, ..., ℓ_k ∧ j = 1, 2, 3} second sample
        θ̂^1 ← (α̂_1, γ̂_1) MLE using s_1
        θ̂^2 ← (α̂_2, γ̂_2) MLE using s_2
        d_p ← d(θ̂^1, θ̂^2)
    p_max ← argmax{d_p}
    s_1^* ← {z_{i,j} : i = 1, ..., p_max ∧ j = 1, 2, 3} first sample
    s_2^* ← {z_{i,j} : i = p_max + 1, ..., ℓ_k ∧ j = 1, 2, 3} second sample
    θ̂_*^1 ← (α̂_1^*, γ̂_1^*) MLE using s_1^*
    θ̂_*^2 ← (α̂_2^*, γ̂_2^*) MLE using s_2^*
    S ← S_φ^h(θ̂_*^1, θ̂_*^2) statistic // using (14)
    Apply the hypothesis test
    if H_0 is rejected then
        (x_q, y_q) is estimated as an edge point
    else
        there is no evidence of edge on the strip
```

There may be cases in which a strip crosses the target's border more than once. This situation may arise in complex, non-convex, shapes. Our current implementation does not handle these cases, since Algorithm 1 will identify the edge of the strongest transition. In future enhancements of this work we will consider an odd amount of border crossings per ray strip and a modification of the interpolation algorithm to cope with these cases. However, as will be shown in the examples, the net effect of this simplified detection is not significant.

3.2. Test Cases

To assess the dependence of the proposed technique on the stochastic distances in its performance, the experimental study consists of both synthetic and actual SAR images. In

the former case, we used the $\mathcal{G}_I^0$ distribution to generate a single look ($L = 1$) and a $L = 2$ image. The image obtained in the multilook case and the actual border of the simulated surface water are shown in Figure 2. The parameter values are $\alpha = -20$ for the simulated lagoon (darker area) and $\alpha \in \{-3, -1.5, -5, -8\}$ for the quadrants Q_I (highly textured zones), Q_{II} (extremely textured regions), Q_{III} (middle textured regions), and Q_{IV} (low textured regions) in which the background is divided. The scale parameter is $\gamma = 0.5$ for the whole image.

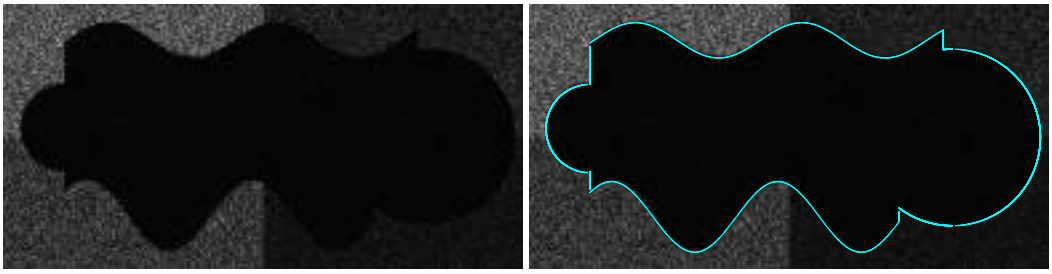

Figure 2. Synthetic image (**left**) with $L = 2$ and the actual border (**right**).

The application to actual SAR images consists of two examples:

1. Three lagoons in the south of Buenos Aires, Argentina, acquired from the SAOCOM mission (see https://catalog.saocom.conae.gov.ar/catalog/, last accessed date: 8 October 2022), 9.22 m resolution, located within the rectangle with geographic coordinates 38°57′41″S 61°27′31″W (left bottom corner) and 38°51′8″S 60°58′20″W (right top corner); see Figure 3. The sizes of the images are 951 × 401, 216 × 106, and 471 × 150 pixels. These lagoons were selected to have a variety of representative examples of different characteristics, such as edge shape, spectral distribution of the backscatter in the water, area, and type of surroundings;
2. Oil spill detection in the zone of the Valdés peninsula, Chubut, Argentina, acquired from COSMO-SkyMed and provided by CONAE; see Figure 4. The image has 1853 × 2111 pixels.

An expert technician manually marked the actual border of the lagoons using high-resolution optical images with full spatial and temporal consistency. Using the same dates is essential in a dynamic problem such as oil spill detection. In this study, we used the option "Historical Imagery" available on the desktop version of Google Earth, to obtain the ROI's view in the desired time.

Algorithm 1 produces a set of points with which the estimated border will be generated using a B-spline approximation. We used two measures to quantify the performance of the estimation in terms of the considered stochastic distance. First, the *Hausdorff distance* defined as $\mathrm{Hd} = \max_{p \in P} \min_{p' \in P'} \|p - p'\|$, where P and P' represent the points in the true border and points obtained by applying our proposal. The smaller Hd is, the better is the edge. Second, the *Intersection over Union* (IoU) is the quotient between the number of pixels in the intersection among the areas defined by the true border and the B-spline curve, and the total of pixels in the union of both areas. The larger IoU is, the better is the edge.

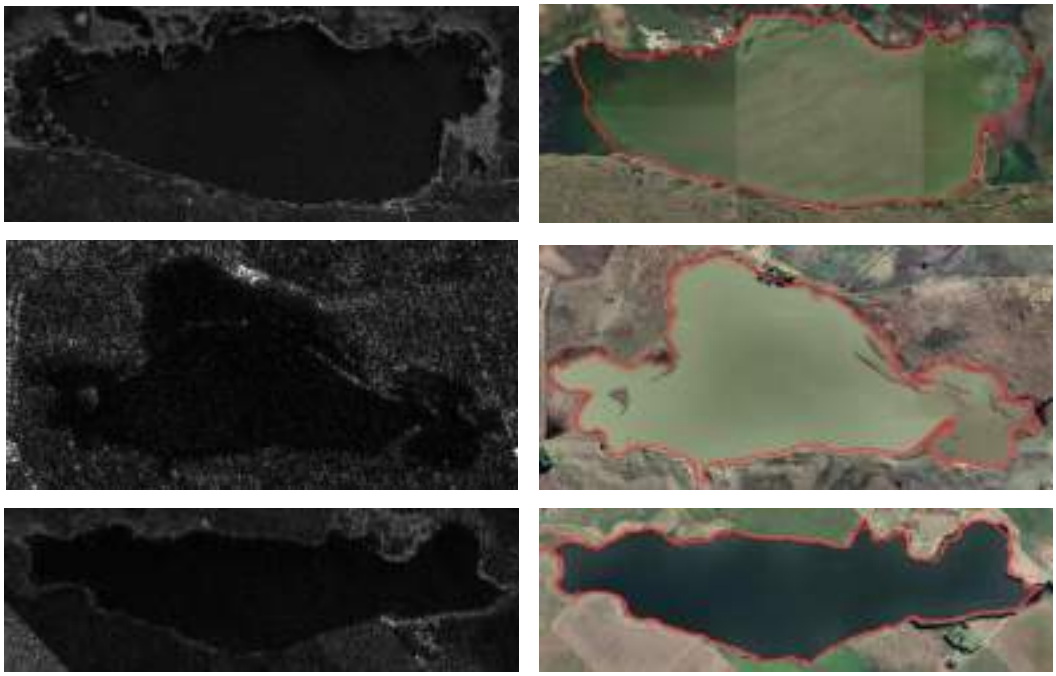

Figure 3. SAOCOM images of lagoons in the south of Buenos Aires, Argentina (**left**), and their true borders (**right**).

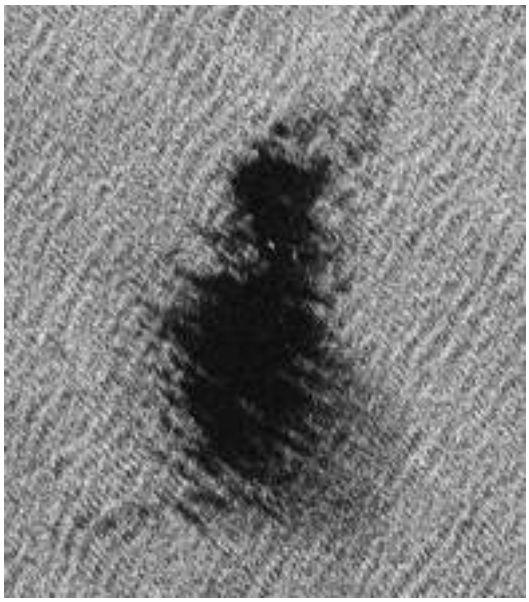

Figure 4. COSMO-SkyMed image of an oil spill.

Since our methodology might detect outliers, we first clean the points obtained in the first execution of the algorithm: we consider the Euclidean distances between two detected points in consecutive rays, and reject those that lie at a distance larger than a specific threshold. The remaining points are considered as inlier estimates. The relevance of rejecting outliers is quantified in Section 4. Figure 5 summarizes the general workflow in the treatment of simulated data. In the case of actual data, the process is the same except that the analysis considers the background as a whole area rather than being divided into quadrants.

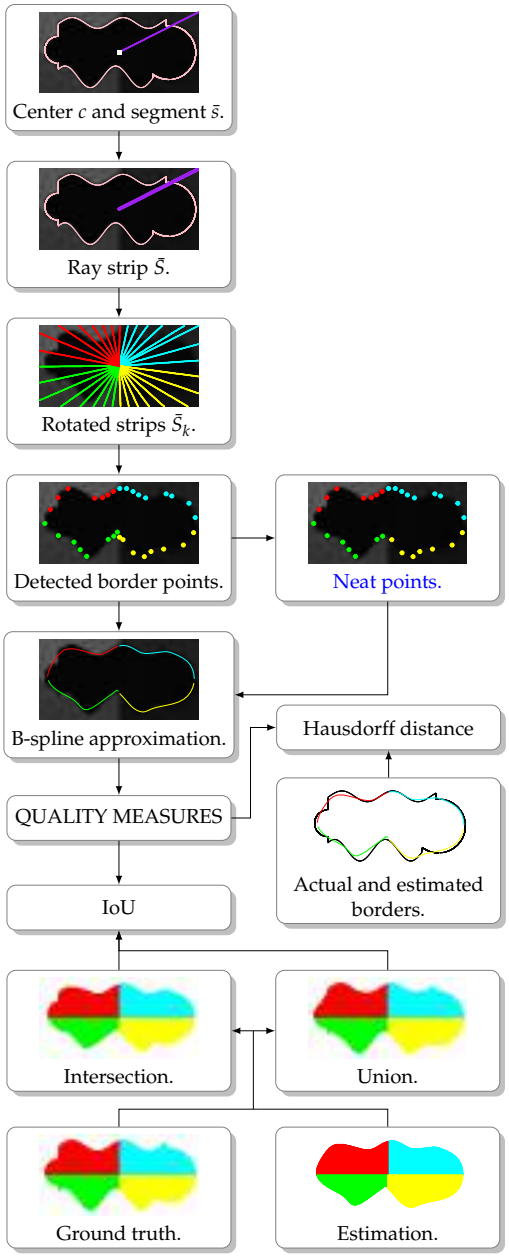

Figure 5. Complete workflow to find the target's border, together with quality assessment.

We used the R platform version 4.1.0 [44] to implement Algorithm 1 and all the additional computations on a personal computer with Intel© Core™ processor, i7-6700K CPU 3.40 GHz, 16 GB RAM, and System Type 64 bit operating system.

4. Results and Discussion

4.1. General Behavior

We first analyze the interplay between texture parameter ($\alpha = -1.5, -3, -5, -8$), number of ray strips ($n_r = 32, 64, 128$), and all points versus "neat" points. The results are shown in Figure 6. Table 2 summarizes these results in the form of recommendations. If the improvement of both quality indicators is balanced, it is recommended to use the neat points to find the B-spline curve.

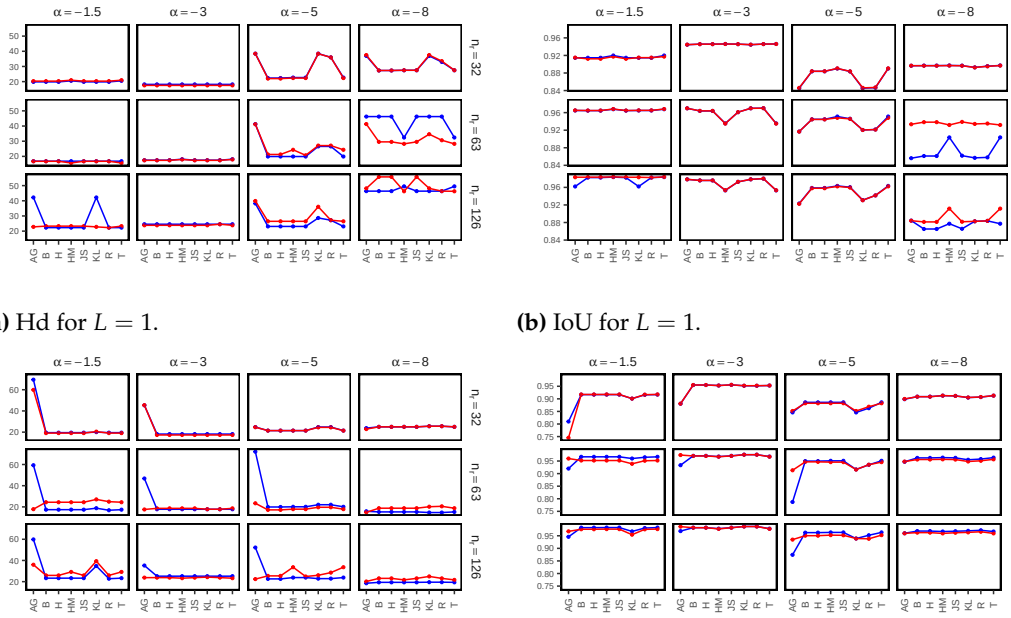

(a) Hd for $L = 1$.

(b) IoU for $L = 1$.

(c) Hd for $L = 2$.

(d) IoU for $L = 2$.

Figure 6. Hausdorff distance (Hd) and Intersection over Union (IoU) for simulated data. Blue and red points represent detected and "neat" points, respectively. Only one line is shown when these results coincide.

Table 2. Cases in which it is recommended to use neat points for the B-spline approximation.

Distance	L	α	n_r
AG	1	−1.5	126
		−3	32
		−8	63
	2	−1.5	63
		−3, −5, −8	126
B	1	−3	32
		−8	63
H	1	−3	32
		−8	63
HM	1	−3	32
		−8	63, 126
JS	1	−3	32
		−8	63
KL	1	−1.5	126
		−3	32
		−8	63
R	1	−3	32
		−8	63
T	1	−3	32
		−8	63, 126

All the considered stochastic distances produced lower Hd when the number of ray strips is equal to 63. On the other hand, a higher value for IoU is obtained when $n_r = 126$, except for $\alpha = -8$ with $L = 1$ where the best performance is achieved by $n_r = 63$. Thus, $n_r = 63$ appears to be the optimal choice for the reduction of computational cost in terms of the required time; cf. Figure 7.

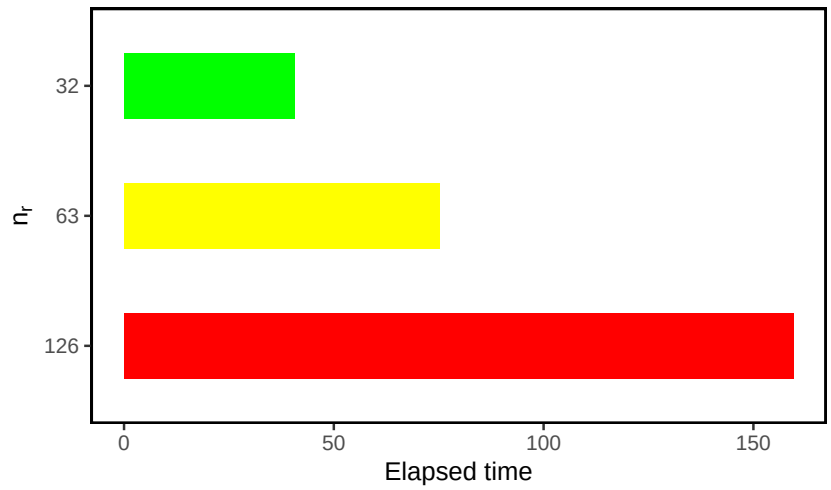

Figure 7. Elapsed time (in seconds) required for the detection algorithm per number of ray strips for synthetic data.

The point L, α for which each stochastic distance achieved the best performance is shown in Table 3. In the single look case, the lowest Hd is reached by HM, KL, R, and T if $\alpha = -3$, and by AG, B, HG, and JS if $\alpha = -8$. Meanwhile, the highest IoU is obtained for $\alpha = -1.5$ for all the stochastic distances, except for AG and KL, which stress if $\alpha = -3$. If $L = 2$. The best results for Hd arise if $\alpha = -8$ for the stochastic distances other than AG with a better performance if $\alpha = -3$. In terms of IoU, the stochastic distances that stand out are AG, KL, and R if $\alpha = -3$, HM and JS if $\alpha = -1.5$, and B and H in both quadrants.

Table 3. Texture parameter in which the results of the detection technique are better according to the stochastic distance for synthetic data.

	$L = 1$		$L = 2$	
Distance	**Hd**	**IoU**	**Hd**	**IoU**
AG	$\alpha = -8$	$\alpha = -3$	$\alpha = -3$	$\alpha = -3$
B	$\alpha = -8$	$\alpha = -1.5$	$\alpha = -8$	$\alpha = -1.5, -3$
H	$\alpha = -8$	$\alpha = -1.5$	$\alpha = -8$	$\alpha = -1.5, -3$
HM	$\alpha = -3$	$\alpha = -1.5$	$\alpha = -8$	$\alpha = -1.5$
JS	$\alpha = -8$	$\alpha = -1.5$	$\alpha = -8$	$\alpha = -1.5$
KL	$\alpha = -3$	$\alpha = -3$	$\alpha = -8$	$\alpha = -3$
R	$\alpha = -3$	$\alpha = -1.5$	$\alpha = -8$	$\alpha = -3$
T	$\alpha = -3$	$\alpha = -1.5$	$\alpha = -8$	$\alpha = -1.5$

Table 4 shows the stochastic distances that have reached the best values for Hd and IoU (see Table 5) depending on the degree of texture and with the considered number of ray strips. In this table, the uncensored points are denoted by D $\in \{$AG, B, H, HM, JS, KL, R, T$\}$, whereas, if outliers are rejected, the "neat" points are denoted by D* with D as above.

Despite the number of possibilities, some differences are explicit. For instance, if the background of a single look image is extremely textured ($\alpha = -1.5$), then the best alternative is to use either HM* or T*; in the case of intermediate texture ($\alpha = -5$), HM and T are more suitable. On the other hand, if $L = 2$ and the background has a low texture degree, then R stems as the best option.

Table 4. Stochastic measures with the best performance per texture for simulated data.

$L = 1$				
α		$n_r = 32$	$n_r = 63$	$n_r = 126$
-1.5	Hd	AG-B-H-JS-KL-R	HM*-T*	B-H-HM-JS-R-T
	IoU	HM-T	HM*-T*	HM*-T*
-3	Hd	HM*-T*	AG*-B*-H*-JS*-KL*-R*	AG*
	IoU	HM-T	R	R
-5	Hd	B*-H*	B-H-HM-JS-T	B-H-HM-JS-T
	IoU	HM*-T*	HM-T	HM-T
-8	Hd	B-H	HM*-T*	HM*-T*
	IoU	HM-T	JS*	T
$L = 2$				
α		$n_r = 32$	$n_r = 63$	$n_r = 126$
-1.5	Hd	B*-H*-HM*-JS*-R*-T*	R	R
	IoU	HM*-T*	B-H-HM-JS-T	HM-JS-T
-3	Hd	B*-H*-HM*-JS*-KL*-R*-T*	AG*	HM*-T*
	IoU	JS	KL-R	R
-5	Hd	B-H-HM-JS-T	B*-H*	AG*
	IoU	B-H-HM-JS-T	HM-JS-T	HM-JS-T
-8	Hd	AG*	KL-R	AG
	IoU	HM*-T*	HM-T	R

Table 5. Best quality measure values and the stochastic distance in which they are achieved for simulated data.

$L = 1$	Stochastic Dist.	Lowest Hd	Stochastic Dist.	Highest IoU
$\alpha = -1.5$	HM*-T*	15.63	HM*-T*	0.984
$\alpha = -3$	AG*-B*-H*-JS*-KL*-R*	17.39	R	0.980
$\alpha = -5$	B-H-HM-JS-T	19.90	HM-T	0.963
$\alpha = -8$	B-H	27.32	JS*	0.939
$L = 2$	**Stochastic Dist.**	**Lowest Hd**	**Stochastic Dist.**	**Highest IoU**
$\alpha = -1.5$	R	16.83	HM-JS-T	0.983
$\alpha = -3$	B*-H*-HM*-JS*-KL*-R*-T*	17.30	R	0.987
$\alpha = -5$	B*-H*	17.18	HM-JS-T	0.963
$\alpha = -8$	KL-R	14.66	R	0.972

4.2. Behavior with Actual Imagery

In the case of SAOCOM data, the estimated number of looks for the images of Figure 3 (left) from top to bottom are $\widehat{L} = 11, 13, 11$. The quality measures are presented in Tables 6–8, where the best values are in bold. The smallest (best) values of Hd for the top left image in Figure 3 are 52.55, if $n_r = 32$, 55.40 if $n_r = 63$, and 64.93 if $n_r = 126$, considering JS. In the case of the middle left image in Figure 3 this minima are 25.35 if $n_r = 32$, 23.87 if $n_r = 63$ and 21.41 if $n_r = 126$, considering HM and T. For the bottom left image in Figure 3 AG* is the stochastic distance that produces the smallest values of Hd for every n_r: 43.98 if $n_r = 32$, 54.15 if $n_r = 63$, and 57.04 if $n_r = 126$. On the other hand, the largest (best) values

of IoU can be summarized as follows. For the top left image in Figure 3: 0.872 ($n_r = 32$) and 0.891 ($n_r = 63$) for HM* and T*; and 0.893 ($n_r = 126$) for JS*. For the middle left image in Figure 3: 0.748 ($n_r = 32$) and 0.734 ($n_r = 63$) for HM and T; and 0.759 ($n_r = 126$) for HM. For the bottom left image in Figure 3: 0.758 ($n_r = 32$) for B and H; 0.767 ($n_r = 63$), and 0.786 ($n_r = 126$) for JS. The Bhattacharyya and Hellinger distances show the same results for Hd and IoU for the three images. The same relation holds between harmonic-mean and triangular distances.

We conclude that the best performance for the images in Figure 3 (left) from top to bottom, are achieved by HM* and T* with $n_r = 63$, HM with $n_r = 126$, and JS with $n_r = 126$, respectively. The estimated borders obtained in these cases are shown in Figures 8–10. The relatively low performance of the SNAP toolbox may be related to excessively conservative algorithms that require strong evidence to identify edges.

Table 6. Quality measure results for the image in Figure 3 top left, for each stochastic distance (SDist).

n_r	SDist	Hd	IoU	SDist	Hd	IoU
32	AG	88.92	0.843	AG*	60.93	0.854
	B	89.24	0.857	B*	53.89	0.871
	H	89.24	0.857	H*	53.89	0.871
	HM	89.24	0.859	HM*	53.89	**0.872**
	JS	89.24	0.858	JS*	**52.55**	0.872
	KL	88.92	0.835	KL*	60.93	0.846
	R	106.64	0.797	R*	61.33	0.841
	T	89.24	0.859	T*	53.89	**0.872**
63	AG	96.21	0.850	AG*	56.65	0.851
	B	96.21	0.879	B*	56.03	0.888
	H	96.21	0.879	H*	56.03	0.888
	HM	96.21	0.871	HM*	57.32	**0.891**
	JS	96.21	0.879	JS*	**55.40**	0.889
	KL	96.21	0.853	KL*	56.65	0.859
	R	99.65	0.838	R*	56.65	0.865
	T	96.21	0.871	T*	57.32	**0.891**
126	AG	95.06	0.861	AG*	67.83	0.872
	B	116.37	0.868	B*	139.14	0.868
	H	116.37	0.868	H*	139.14	0.868
	HM	116.37	0.861	HM*	133.73	0.863
	JS	94.96	0.880	JS*	**64.93**	**0.893**
	KL	95.06	0.865	KL*	67.83	0.877
	R	95.06	0.845	R*	66.72	0.880
	T	116.37	0.861	T*	133.73	0.863
SNAP		78.52	0.813	-	-	-

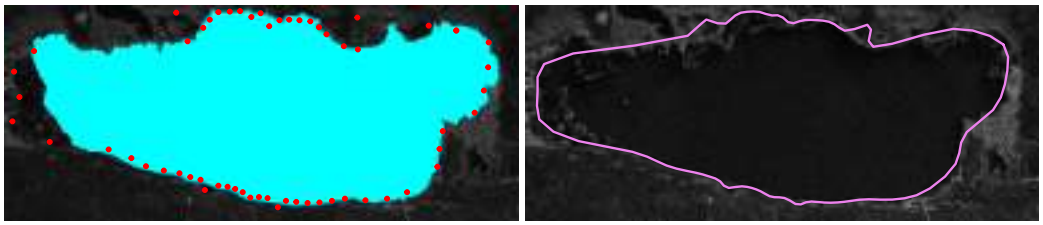

(a) Ground truth and detected border points. **(b)** B-spline approximation.

Figure 8. Results of HM* and T* with $n_r = 63$ when the proposed algorithm is applied to the first lagoon in Figure 3 (left).

Table 7. Quality measure results for the image in Figure 3 middle left, for each stochastic distance (SDist).

n_r	SDist	Hd	IoU	SDist	Hd	IoU
32	AG	38.97	0.572	AG*	55.81	0.528
	B	29.44	0.683	B*	55.81	0.639
	H	29.44	0.683	H*	55.81	0.639
	HM	**25.35**	**0.748**	HM*	**25.35**	**0.748**
	JS	29.44	0.680	JS*	55.81	0.636
	KL	37.78	0.602	KL*	55.81	0.557
	R	29.44	0.674	R*	55.81	0.630
	T	**25.35**	**0.748**	T*	**25.35**	**0.748**
63	AG	27.76	0.616	AG*	34.89	0.568
	B	28.96	0.704	B*	28.96	0.704
	H	28.96	0.704	H*	28.96	0.704
	HM	**23.87**	0.729	HM*	25.51	**0.734**
	JS	28.96	0.705	JS*	28.96	0.705
	KL	28.96	0.645	KL*	33.89	0.618
	R	28.96	0.694	R*	28.96	0.694
	T	**23.87**	0.729	T*	25.51	**0.734**
126	AG	26.87	0.678	AG*	28.95	0.708
	B	25.59	0.748	B*	25.59	0.748
	H	25.59	0.748	H*	25.59	0.748
	HM	**21.41**	**0.759**	HM*	29.22	0.751
	JS	25.24	0.749	JS*	25.24	0.749
	KL	25.24	0.693	KL*	27.33	0.705
	R	25.59	0.735	R*	25.59	0.735
	T	**21.41**	0.758	T*	29.22	0.750
SNAP		21.40	0.755	-	-	-

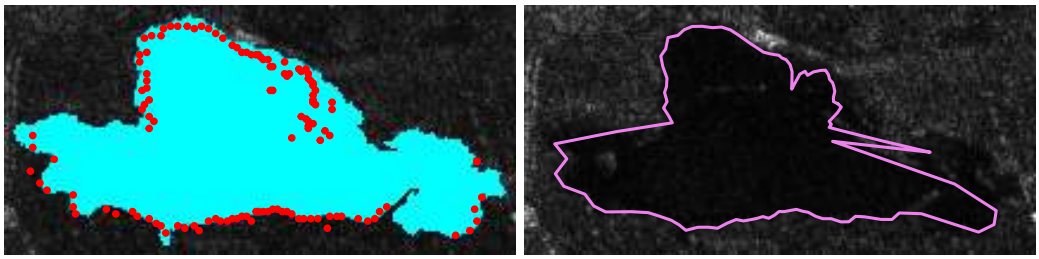

(a) Ground truth and detected border points. **(b)** B-spline approximation.

Figure 9. Results of HM with $n_r = 126$ when the proposed algorithm is applied to the second lagoon in Figure 3 (left).

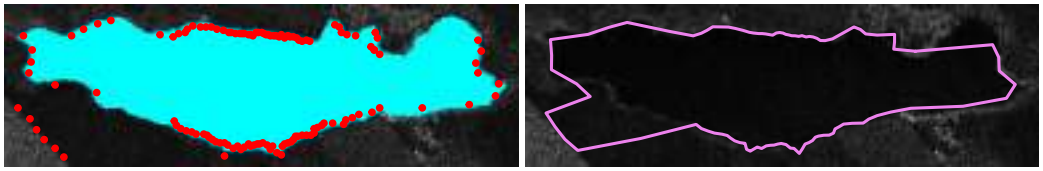

(a) Ground truth and detected border points. **(b)** B-spline approximation.

Figure 10. Results of JS with $n_r = 126$ when the proposed algorithm is applied to the third lagoon in Figure 3 (left).

Table 8. Quality measure results for the image in Figure 3 bottom left, for each stochastic distance (SDist).

n_r	SDist	Hd	IoU	SDist	Hd	IoU
32	AG	**43.98**	0.752	AG*	**43.98**	0.750
	B	**43.98**	**0.758**	B*	149.36	0.579
	H	**43.98**	**0.758**	H*	149.36	0.579
	HM	279.32	0.014	HM*	279.32	0.014
	JS	**43.98**	0.756	JS*	149.57	0.577
	KL	**43.98**	0.752	KL*	**43.98**	0.750
	R	**43.98**	0.754	R*	**43.98**	0.752
	T	279.32	0.014	T*	279.32	0.014
63	AG	54.74	0.740	AG*	**54.15**	0.726
	B	55.01	0.766	B*	55.26	0.751
	H	55.01	0.766	H*	55.26	0.751
	HM	55.01	0.758	HM*	55.26	0.744
	JS	54.74	**0.767**	JS*	**54.15**	0.752
	KL	54.74	0.762	KL*	**54.15**	0.747
	R	55.01	0.761	R*	55.26	0.746
	T	55.01	0.758	T*	55.26	0.744
126	AG	**57.04**	0.756	AG*	**57.04**	0.756
	B	58.05	0.786	B*	58.52	0.770
	H	58.05	0.786	H*	58.52	0.770
	HM	58.05	0.778	HM*	58.52	0.763
	JS	**57.04**	**0.786**	JS*	57.09	0.763
	KL	**57.04**	0.776	KL*	57.06	0.773
	R	58.05	0.783	R*	57.63	0.780
	T	58.05	0.778	T*	58.52	0.763
SNAP		58.94	0.669	-	-	-

To compare the performance of our proposal with other available methods, we applied the fractional Land/Water mask provided by SeNtinel Applications Platform (SNAP) from the European Space Agency (ESA) (https://step.esa.int/, last accessed date: 8 October 2022). The estimated borders are shown in Figure 11 and the quality measures at the bottom row of Tables 6–8. Even though the results are good, they do not succeed as the best ones obtained by our methodology.

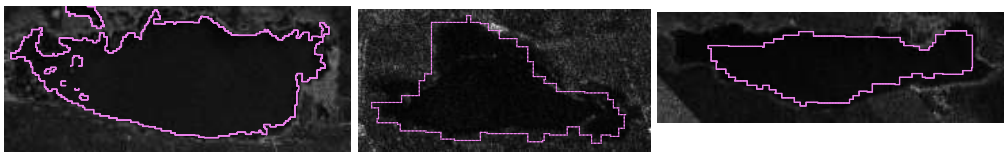

(a) Top left figure. **(b)** Middle left figure. **(c)** Right left figure.

Figure 11. Estimated borders and quality measures obtained with the SNAP toolbox applied to the images of Figure 3.

It is noteworthy that, in Table 7, the smallest best IoU is 0.759. The user may decide to increase or decrease the number of points if he/she uses IoU as the definitive measure of performance. The estimated number of looks equals 3 in the image shown in Figure 4. The results obtained when applying our proposal with $n_r = 63$ and using the neat points are shown in Figure 12. It can be noticed that the performance of AG and KL is not acceptable. The behavior of B and H is the same; meanwhile, HM and T produce identical results. By visual inspection, the performance of B, H, and JS are suitable to detect the contour of the oil spill.

One aspect of the methodology is determining an appropriate amount of radii as a trade-off between the effectiveness and the computational cost. Increasing this number above 63 radii in all the experiments did not generate any further enhancement, so

$n_r = 63$ was selected as the best parameter. In monopolarimetric images, the selection of the stochastic distance strongly depends on the degree of the texture of the area around the water body. The Harmonic-Mean, Rényi, and Triangular distances are the best options for extremely textured regions, while the Kullback–Leibler distance is the best for the highly textured zones. In the case of mildly textured areas, the optimal distance evaluation does not point to any preferred choice. Finally, applying the proposal to actual SAR images produced the best results with the Harmonic-Mean and Triangular distances in all the regions of interest concerning lagoons. In the case of dealing with oil spill detection, Bhattacharyya, Hellinger, and Jensen–Shannon distances are recommended. It is worth remarking that the procedure to neat points for the B-spline approximation generated better results in general, without a significant increase in the computational cost.

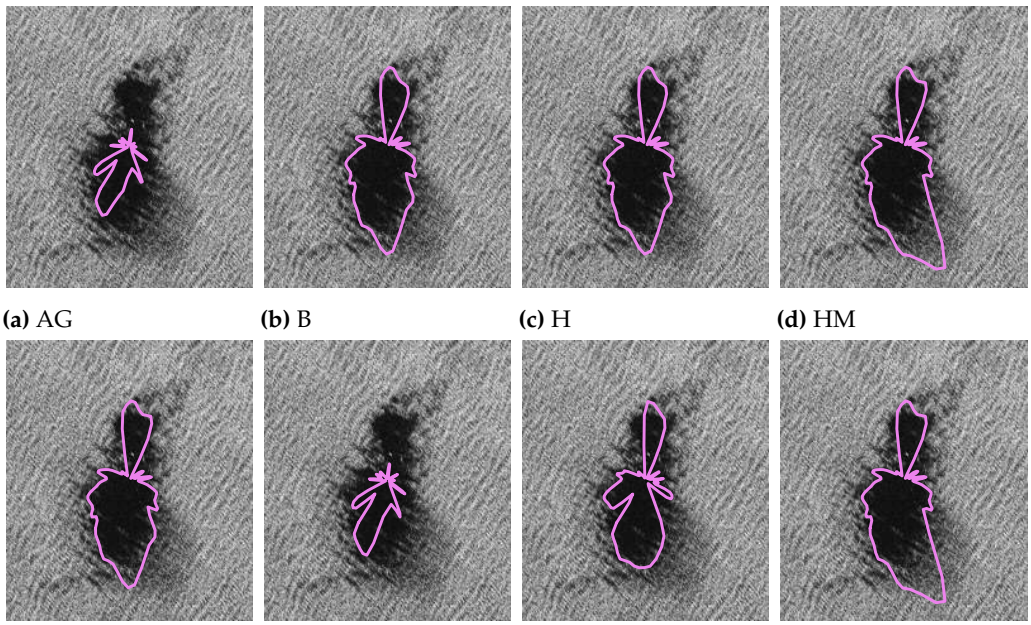

(a) AG **(b)** B **(c)** H **(d)** HM

(e) JS **(f)** KL **(g)** R **(h)** T

Figure 12. B-spline curves from the inlier points obtained by the proposed algorithm applied to the image of Figure 4, for each stochastic distance and $n_r = 63$.

Since the $\mathcal{G}_I^0$ distribution is based on the product of the backscatter and the speckle noise, this effect is inherent to our proposal. Notice that we do not reduce the speckle but use the information provided by it. On the other hand, our approach uses a test statistic; if there is no evidence of change, no point will be detected and the edge will be estimated by an approximation with those points that provide evidence of change. We provide an assessment of the performance of the technique after approximating the edge with a spline curve, and not of the accuracy of individual points.

5. Conclusions

Water recognition is an essential task in diverse fields of knowledge, such as biological environment, climate, earthly disasters, agriculture, and tourism, among others. This information can be used either to improve the production of natural resources or to prevent damages caused by contamination, floods, and droughts.

The present work proposed an automated segmentation algorithm suited for small water bodies. First, candidate border points are detected along radial transects, taking into account the change in statistical properties of the images, implemented through a hypothesis test based on stochastic distances between $\mathcal{G}_I^0$ distributions. Then, the estimated border is obtained when these points, or the set of these points that are not rejected as outliers, are used to define the B-splines curves. To select the most suitable

stochastic distance, the suggested technique was performed using Arithmetic-Geometric, Bhattacharyya, Hellinger, Harmonic-Mean, Jensen–Shannon, Kullback-Leibler, Rényi, and Triangular distances. The method was tested both with simulated SAR images comparing different roughness levels and with four actual COSMO-SkyMed SAR images obtained from the SAOCOM/SIASGE constellation. Considering the ground truth border marked by an expert (in those cases, an optical version of the image was available) and the approximation attained, the results obtained were evaluated by computing the Hausdorff distance and the Intersection over Union.

The results suggest Harmonic-Mean and Triangular as the most suitable stochastic distances for lagoons' border detection, and Bhattacharyya, Hellinger, and Jensen–Shannon for oil spill, using 63 ray strips and only points that are not rejected as outliers in all cases. Our approach relies on the assumption that different targets exhibit distinct statistical properties. If the models cannot retrieve such information, other features must be used. In future work, we are interested in studying this methodology's extensions and modifications to other regions in SAR imagery with the purpose of a general segmentation algorithm. In addition, we will extend our proposal to handle non-convex targets.

Author Contributions: Conceptualization, A.R., A.C.F., and C.D.; methodology, A.R., N.R.S., A.C.F., and C.D.; software, A.R. and N.R.S.; validation, A.R., A.C.F., and C.D.; formal analysis, A.R., A.C.F., and C.D.; investigation, A.R., N.R.S., A.C.F., and C.D.; resources, N.R.S.; data curation, A.R. and N.R.S.; writing—original draft preparation, A.R., A.C.F., and C.D.; writing—review and editing, A.R., A.C.F., and C.D.; visualization, A.R.; supervision, A.C.F. and C.D.; project administration, A.R.; funding acquisition, A.C.F. and C.D. All authors have read and agreed to the published version of the manuscript.

Funding: Grant 24/K083 of the Universidad Nacional del Sur.

Data Availability Statement: The R implementation of this method, together with the presented examples, will be made publicly available upon acceptance of the manuscript.

Acknowledgments: This work partially was supported by Grant PID ASUTNBA0005149 of the Universidad Tecnológica Nacional.

Conflicts of Interest: The authors declare no conflict of interest.

References

1. Biggs, J.; Von Fumetti, S.; Kelly-Quinn, M. The importance of small waterbodies for biodiversity and ecosystem services: Implications for policy makers. *Hydrobiologia* **2017**, *793*, 3–39. https://doi.org/10.1007/s10750-016-3007-0.
2. Al Fugura, A.; Billa, L.; Pradhan, B. Semi-automated procedures for shoreline extraction using single RADARSAT-1 SAR image. *Estuar. Coast. Shelf Sci.* **2011**, *95*, 395–400. https://doi.org/10.1016/j.ecss.2011.10.009.
3. Bao, L.; Lv, X.; Yao, J. Water extraction in SAR images using features analysis and dual-threshold graph cut model. *Remote Sens.* **2021**, *13*, 3465. https://doi.org/10.3390/rs13173465.
4. Hong, S.; Jang, H.; Kim, N.; Sohn, H.G. Water area extraction using RADARSAT SAR imagery combined with LANDSAT imagery and terrain information. *Sensors* **2015**, *15*, 6652–6667. https://doi.org/10.3390/s150306652.
5. Lv, W.; Yu, Q.; Yu, W. Water extraction in SAR images using GLCM and support vector machine. In Proceedings of the IEEE 10th International Conference on Signal, Beijing, China 24–28 October 2010; pp. 740–743. https://doi.org/10.1109/ICOSP.2010.5655766.
6. Markert, K.N.; Chishtie, F.; Anderson, E.R.; Saah, D.; Griffin, R.E. On the merging of optical and SAR satellite imagery for surface water mapping applications. *Results Phys.* **2018**, *9*, 275–277. https://doi.org/10.1016/j.rinp.2018.02.054.
7. Meng, Q.; Wen, X.; Yuan, L.; Xu, H. Factorization-based active contour for water-land SAR image segmentation via the fusion of features. *IEEE Access* **2019**, *7*, 40347–40358. https://doi.org/10.1109/ACCESS.2019.2905847.
8. Niedermeier, A.; Romaneessen, E.; Lehner, S. Detection of coastlines in SAR images using wavelet methods. *IEEE Trans. Geosci. Remote Sens.* **2000**, *38*, 2270–2281. https://doi.org/10.1109/36.868884.
9. Zhang, Z.; Lu, H.; Zhao, M. Water body extraction and change detection based on multi-temporal SAR images. In Proceedings of the MIPPR 2009: Remote Sensing and GIS Data Processing and Other Applications. *Int. Soc. Opt. Photonics*, **2009**, *7498*, 74982P. https://doi.org/10.1117/12.834100.
10. Zheng, X.; Chen, J.; Zhang, S.; Chen, J. Water extraction of SAR image based on region merging algorithm. In Proceedings of the 2017 International Applied Computational Electromagnetics Society Symposium (ACES), Firenze, Italy, 26–30 March 2017; pp. 1–2.

11. Janati, M.; Kolahdoozan, M.; Imanian, H. Artificial neural network modeling for the management of oil slick transport in the marine environments. *Pollution* **2020**, *6*, 399–415.
12. Vasconcelos, R.N.; Lima, A.T.C.; Lentini, C.A.D.; Miranda, G.V.; Mendonça, L.F.; Silva, M.A.; Cambuí, E.C.B.; Lopes, J.M.; Porsani, M.J. Oil spill detection and mapping: A 50-year bibliometric analysis. *Remote Sens.* **2020**, *12*, 3647.
13. Mohammadi, M.; Sharifi, A.; Hosseingholizadeh, M.; Tariq, A. Detection of oil pollution using SAR and optical remote sensing imagery: A case study of the Persian Gulf. *J. Indian Soc. Remote Sens.* **2021**, *49*, 2377–2385.
14. Li, Y.; Lyu, X.; Frery, A.C.; Ren, P. Oil Spill Detection with Multiscale Conditional Adversarial Networks with Small-data Training. *Remote Sens.* **2021**, *13*(12) . https://doi.org/10.3390/rs13122378.
15. Kuck, T.N.; Gomez, L.D.; Sano, E.E.; Bispo, P.d.C.; Honorio, D.D.C. Performance of Speckle Filters for COSMO-SkyMed Images From the Brazilian Amazon. *IEEE Geosci. Remote Sens. Lett.* **2022**, *19* , 1–5. https://doi.org/10.1109/LGRS.2021.3057263.
16. Almulihi, A.; Alharithi, F.; Bourouis, S.; Alroobaea, R.; Pawar, Y.; Bouguila, N. Oil spill detection in SAR images using online extended variational learning of dirichlet process mixtures of gamma distributions. *Remote Sens.* **2021**, *13*, 2991.
17. Delrieux, C.A.; Odorico, P.; Rodríguez, L.; Cipolletti, M.P.; Marcovecchio, D. Real-time vessel and oil spill detection in the argentine ocean littoral using SAR satellite imagery. *Indian J. Mar. Sci.* **2016** , *45*, 1101–1109.
18. Gauthier, M.F.; Weir, L.; Ou, Z.; Arkett, M.; De Abreu, R. Integrated satellite tracking of pollution: A new operational program. In Proceedings of the 2007 IEEE International Geoscience and Remote Sensing Symposium, Barcelona, Spain, 23–28 July 2007; pp. 967–970. https://doi.org/10.1109/IGARSS.2007.4422960.
19. Mera, D.; Bolon-Canedo, V.; Cotos, J.M.; Alonso-Betanzos, A. On the use of feature selection to improve the detection of sea oil spills in SAR images. *Comput. Geosci.* **2017**, *100*, 166–178. https://doi.org/10.1016/j.cageo.2016.12.013.
20. Blake, A.; Isard, M. *Active Contours*; Springer: Berlin/Heidelberg, Germany, 1998. https://doi.org/10.1007/978-1-4471-1555-7.
21. Gonzalez, R.C.; Woods, R.E. *Digital Image Processing*, 3rd ed.; Addison-Wesley: Reading, MA, USA, 1992.
22. Gambini, J.; Mejail, M.; Jacobo-Berlles, J.; Frery, A.C. Feature extraction in speckled imagery using dynamic B-spline deformable contours under the $\mathcal{G}^0$ model. *Int. J. Remote Sens.* **2006**, *27*, 5037–5059. https://doi.org/10.1080/01431160600702616.
23. Gambini, J.; Mejail, M.; Jacobo-Berlles, J.; Frery, A.C. Accuracy of edge detection methods with local information in speckled imagery. *Stat. Comput.* **2008**, *18*, 15–26. https://doi.org/10.1007/s11222-007-9034-y.
24. Frery, A.C.; Jacobo-Berlles, J.; Gambini, J.; Mejail, M. Polarimetric SAR image segmentation with B-splines and a new statistical model. *Multidimens. Syst. Signal Process.* **2010**, *21*, 319–342. https://doi.org/10.1007/s11045-010-0113-4.
25. Nascimento, A.D.C.; Horta, M.M.; Frery, A.C.; Cintra, R.J. Comparing edge detection methods based on stochastic entropies and distances for PolSAR imagery. *IEEE J. Sel. Top. Appl. Earth Obs. Remote Sens.* **2014**, *7*, 648–663. https://doi.org/10.1109/JSTARS.2013.2266319.
26. Naranjo-Torres, J.A.; Gambini, J.; Frery, A.C. The geodesic distance between $\mathcal{G}_I^0$ models and its application to region discrimination. *IEEE J. Sel. Top. Appl. Earth Obs. Remote Sens.* **2017**, *10*, 987–997. https://doi.org/10.1109/JSTARS.2017.2647846.
27. Girón, E.; Frery, A.C.; Cribari-Neto, F. Nonparametric edge detection in speckled imagery. *Math. Comput. Simul.* **2012**, *82*, 2182–2198. https://doi.org/10.1016/j.matcom.2012.04.013.
28. Nascimento, A.D.C.; Cintra, R.J.; Frery, A.C. Hypothesis testing in speckled data with stochastic distances. *IEEE Trans. Geosci. Remote Sens.* **2009**, *48*, 373–385. https://doi.org/10.1109/TGRS.2009.2025498.
29. Revollo, N.V.; Frery, A.C.; Delrieux, C.A. Detección de derrames de hidrocarburo basada en kernel radial automático (in Spanish). In Proceedings of the XVIII Reunión de Trabajo en Procesamiento de la Información y Control , Bahía Blanca, Buenos Aires, Argentina, 18–20 September 2019; pp. 169–173.
30. Yue, D.X.; Xu, F.; Frery, A.C.; Jin, Y.Q. SAR image statistical modeling Part I: single-pixel statistical models. *IEEE Geosci. Remote Sens. Mag.* **2021**, *9*, 82–114. https://doi.org/10.1109/MGRS.2020.3004508.
31. Frery, A.C.; Muller, H.J.; Yanasse, C.d.C.F.; Sant'Anna, S.J.S. A model for extremely heterogeneous clutter. *IEEE Trans. Geosci. Remote Sens.* **1997**, *35*, 648–659. https://doi.org/10.1109/36.581981.
32. Casella, G.; Berger, R.L. *Statistical Inference*; Duxbury: Pacific Grove, CA, USA , 2002; Volume 2.
33. Oliver, C.; Quegan, S. *Understanding Synthetic Aperture Radar Images*; SciTech Publishing: Raleigh, NC, USA, 2004.
34. Salicrú, M.; Morales, D.; Menéndez, M.L.; Pardo, L. On the applications of divergence type measures in testing statistical hypotheses. *J. Multivar. Anal.* **1994**, *51*, 372–391. https://doi.org/10.1006/jmva.1994.1068.
35. Burbea, J.; Rao, C.R. Entropy differential metric, distance and divergence measures in probability spaces: A unified approach. *J. Multivar. Anal.* **1982**, *12*, 575–596. https://doi.org/10.1016/0047-259X(82)90065-3.
36. Taneja, I.J. New developments on generalized information measures. *Adv. Imaging Electron Phys.* **1995**, *91*, 37–141. https://doi.org/10.1016/S1076-5670(08)70106-X.
37. Bhattacharyya, A. On a measure of divergence between two statistical populations defined by their probability distributions. *Bull. Calcutta Math. Soc.* **1943**, *35*, 99–109.
38. Hellinger, E. Neue begründung der theorie quadratischer formen von unendlichvielen veränderlichen. *J. FÜR Die Reine Und Angew. Math.* **1909**, *1909*, 210–271.
39. Taneja, I.J. Bounds on triangular discrimination, harmonic mean and symmetric chi-square divergences. *arXiv* **2005**, arXiv:math/0505238.

40. Lin, J. Divergence measures based on the Shannon entropy. *IEEE Trans. Inf. Theory* **1991**, *37*, 145–151. https://doi.org/10.1109/18.61115.
41. Kullback, S.; Leibler, R.A. On information and sufficiency. *Ann. Math. Stat.* **1951**, *22*, 79–86. https://doi.org/10.1214/aoms/1177729694.
42. Rényi, A. On measures of entropy and information. In *Proceedings of the Fourth Berkeley Symposium on Mathematical Statistics and Probability: Contributions to the Theory of Statistics*; The Regents of the University of California: Oakland, CA, USA, 1961; Volume 1, pp. 547–561.
43. Bresenham, J.E. Algorithm for computer control of a digital plotter. *IBM Syst. J.* **1965**, *4*, 25–30. https://doi.org/10.1147/sj.41.0025.
44. R Core Team. R: A language and environment for statistical computing (R Version 4.0. 3, R Foundation for Statistical Computing, Vienna, Austria, 2020), 2021. Avaliable online: https://www.R-project.org/, last access date: 8 October 2022.